Review of Scientific Instruments

Construction of a gigahertz-bandwidth radio-frequency scanning tunneling microscope based on a commercial low-temperature system

Cite as: Rev. Sci. Instrum. **90**, 103706 (2019); https://doi.org/10.1063/1.5109721
Submitted: 13 May 2019 . Accepted: 23 September 2019 . Published Online: 14 October 2019

Chaoqiang Xu, Yande Que, Yuan Zhuang, Kedong Wang, and Xudong Xiao

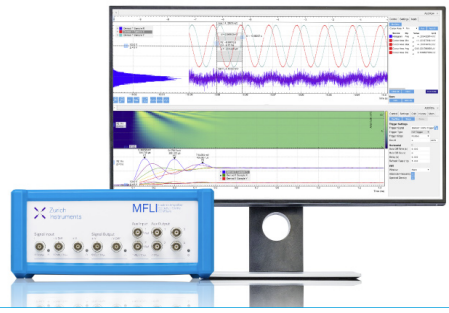

AIP Publishing

Review of Scientific Instruments ARTICLE scitation.org/journal/rsi

Construction of a gigahertz-bandwidth radio-frequency scanning tunneling microscope based on a commercial low-temperature system

Cite as: Rev. Sci. Instrum. 90, 103706 (2019); doi: 10.1063/1.5109721
Submitted: 13 May 2019 • Accepted: 23 September 2019 •
Published Online: 14 October 2019

Chaoqiang Xu,[1] Yande Que,[1] Yuan Zhuang,[1] Kedong Wang,[2,3] and Xudong Xiao[1,a)]

AFFILIATIONS

[1] Department of Physics, The Chinese University of Hong Kong, Shatin, Hong Kong, China
[2] Department of Physics, Southern University of Science and Technology, Shenzhen, Guangdong 518055, People's Republic of China
[3] Shenzhen Key Laboratory of Quantum Science and Engineering, SUSTech, Shenzhen 518055, China

[a)] **Author to whom correspondence should be addressed:** xdxiao@phy.cuhk.edu.hk

ABSTRACT

The highest frequency of the electric signal that a conventional scanning tunneling microscope (STM) can process typically lies in the kilohertz regime, imposing a limitation on its temporal resolution to the submillisecond regime. When extracting (feeding) the high frequency, or radio-frequency (RF), signal out of (into) the tunnel junction, the most challenging part is that the tunnel junction has a very high impedance, causing significant reflections. Here, we present a systematic solution on the construction of RF-STM with high sensitivity. To minimize radiation loss, using coaxial cables as conducting wires, we designed an active impedance matching network (IMN) based on a field-effect transistor, which can provide impedance matching over a wide frequency range and can bridge the enormous impedance difference associated with the tunnel junction. To shorten the signal cable before amplification, the STM probe itself was directly mounted on the IMN as the input pin, which is an unprecedented attempt to minimize the undesired parasitic capacitances. Furthermore, we employed a two-stage cryogenic SiGe low noise amplifier and a high-end spectrum analyzer to amplify and subsequently analyze the RF signal of interest. After this systematic engineering, the bandwidth of our STM has been improved to the gigahertz regime, implying a six orders of magnitude improvement. The sensitivity level of our newly built RF-STM is measured to be better than 1.0 pA/$\sqrt{\text{Hz}}$ at 200 MHz at 78 K. The RF-STM also finds its application in nanoscale thermometry. Our efforts in its instrumentation should contribute to the development of high frequency scanning tunneling microscopy.

I. INTRODUCTION

The scanning tunneling microscope (STM) has become a powerful surface analysis tool since its invention in 1981.[1,2] Employing the tunneling electrons as the probe, which is sensitive to the tip-sample separation distance and localized density of states (LDOS), the STM can obtain an atomically resolved topography image and localized electronic structure of the conducting surface.[3–8] However, a conventional STM mainly focuses on the low-frequency (DC) component of the tunneling current, regarding the high-frequency component as undesired noise. The typical bandwidth of a STM is below 10 kHz, determined by the tunnel resistance and the stray capacitance, which is far below the fundamental limit, namely, the tunneling rate of electrons flowing through the tip-sample junction (for a tunneling current I_T of 160 pA, the tunneling rate is given by $I_T/e \sim 1$ GHz). This incompatibility renders the STM low temporal resolution, hence leading to the need for development of a high frequency STM or radio-frequency (RF) STM.[9] In 2007, Kemiktarak *et al.* developed a RF-STM with an electronic bandwidth as high as 10 MHz by utilizing a resonant LC circuit. This RF-STM allowed for high-speed STM imaging and nanoscale thermometry.[9] Another application example of the RF-STM is referred to as the electron spin resonance (ESR) STM.[10,11] Pioneered by Manassen, the ESR-STM is sensitive enough to detect the precession of

individual surface spins at a small static magnetic field, manifested as an elevated current noise at a high frequency.[10] Recently, Müllegger *et al.* reported the observation of oscillation of the molecular-chain formed by organic radical α,γ-bisdiphenylene-β-phenylallyl (BDPA) molecules where the oscillating molecular-chain periodically modulates the tip-sample separation distance and thus induces an observable RF signal to be detected by the RF-STM.[12] The RF-STM opens a new window to study various dynamic processes of physical systems at nanometer scale. On the other hand, actively applying RF power to the tunneling junction offers an opportunity to detect and manipulate the quantum states of surface spins.[13–16] The construction of a RF-STM requires a significant modification on the circuitry. However, few papers have been published on the instrumental development of such RF-STM.[9,17]

In this work, the construction of the RF-STM is based on a commercial Omicron low temperature (LT) STM in our lab. Detailed technical solutions are presented to target specific instrumental issues, including the replacement of unshielded wires, the design of active impedance matching network (IMN), namely, a buffer amplifier with an internal bias tee, and the installation of the high-end cryogenic RF amplifiers and the spectrum analyzer. After the instrumental modifications, the performance of the constructed RF-STM concerning the basic operation of STM imaging and the sensitivity level in the RF band are tested. The sensitivity is better than 1.0 pA/$\sqrt{}$Hz at 200 MHz at 78 K and can be further improved by a factor of 4–5 through cooling down the sample to 4.3 K.

II. CONSTRUCTION OF RF-STM

A. Overview of the constructed RF-STM

As shown in Fig. 1(a), a conventional STM is essentially composed of a sharp probe tip, which is magnetically attached on the top of the scanner tube (a piezodrive); a sample, which contains the surface of interest; and the STM electronics, which provide the sample bias, read the amplified tunneling current, and apply the periodic ramping voltages on the piezodrive during scanning. In practice, the STM is usually housed in the UHV and cryogenic environment to avoid contamination and suppress thermal noise. Upgrading the STM to a RF-STM requires a complete modification on the STM circuitry, as illustrated by Fig. 1(b).

First of all, for the transmission of the RF signal in the STM, all of the wires including the gap voltage wire and tunneling current wire should be replaced with 50 Ω coaxial cables terminated with specific connectors [in our equipment, SubMiniature version A (SMA) and SubMiniature Push-on Micro (SMPM) connectors are used] whose characteristic impedances are also 50 Ω. In particular, the replacement of gap voltage wire and installation of the bias Tee and RF signal generator, as shown in Fig. 1(b), provide an optional active RF electric field for the tunnel junction, which makes our RF-STM more versatile in future explorations of RF-related phenomena at nanoscales.

Second, to increase the S/N ratio, a delicate signal recovery system is installed on the STM equipment. It consists of a buffer

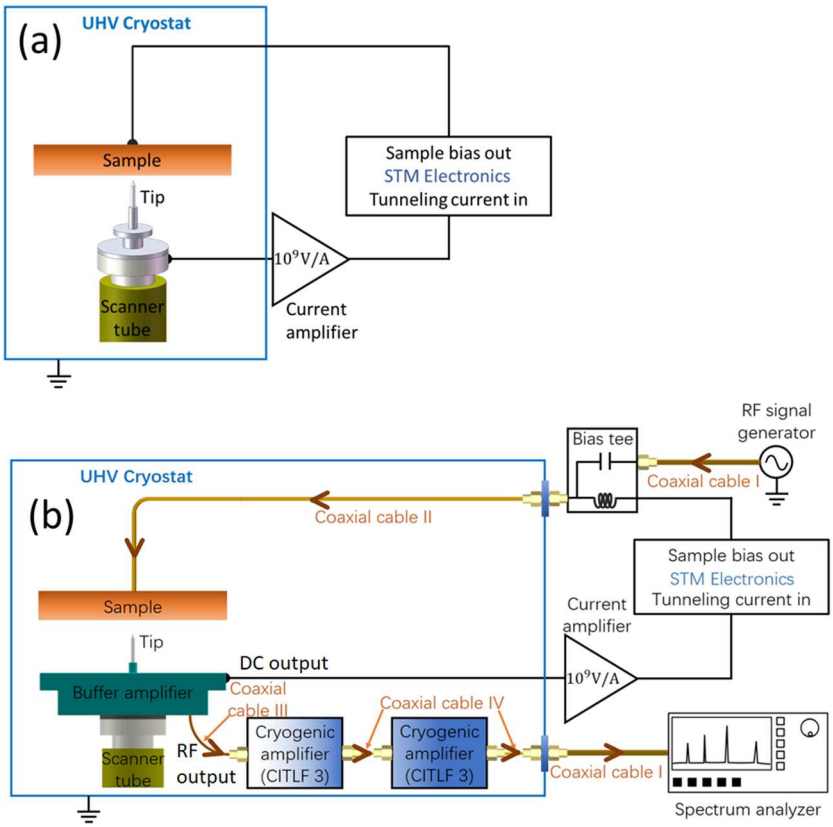

FIG. 1. Schematic diagrams of (a) a conventional STM and (b) our RF-STM, where the flow direction of the RF signal is denoted by the brown arrows.

amplifier on which the probe tip is attached, two subsequent cryogenic amplifiers in series (total power gain: ~60 dB) from Cosmic Microwave Technology, Inc., and a high-end spectrum analyzer from Rohde & Schwarz (FSW-8 signal analyzer, bandwidth: 8 GHz; display average noise level: −166 dBm/Hz at 1 GHz with the preamplifier option).

Third, owing to the nature of large impedance of the tunnel junction, most of the RF signal would be reflected. Therefore, an impedance matching network is indispensable in the signal recovery system. A simple approach is to insert a L-section consisting of one capacitor and one inductor between the tunnel junction and the cryogenic amplifier with 50 Ω input impedance. However, this approach can only provide a good impedance matching in a quite narrow bandwidth around a specific center frequency. Nonetheless, many groups adopted this method in their equipment,[9–11] which, in our opinion, may produce some spurious "signals." An alternative approach is to employ a field effect transistor (FET) that, on the contrary, can provide an acceptable impedance matching over a very wide bandwidth (typically, 10–1000 MHz) despite the obvious difficulties in the implementation, for example, power supply for the FET. Several groups have demonstrated the feasibility of this method in ESR-STM experiments despite a large power consumed by the FET.[18,19] In many cases, it is very difficult to predict the exact positions of the RF signal of interest. Thus, we decide to develop a broadband impedance matching network based on FET. It will be noted that our buffer amplifier indeed serves as the crucial impedance matching network.

In the following, several important steps in this upgrade work will be presented with details.

B. Installation of coaxial cable assemblies

In our RF-STM equipment, all of the electronic devices, such as the RF signal generator, the bias tee, the buffer amplifier, cryogenic amplifiers, and the spectrum analyzer, have an input impedance of 50 Ω and are connected by 50 Ω coaxial cable assemblies. The coaxial cable assemblies consist of the coaxial cable with certain length and two specific RF connectors on both ends. As shown in Fig. 1(b), four kinds of coaxial cable assemblies are used in our upgrade.

At the air side of the setup, two coaxial cable assemblies are used: one connects the RF signal generator to the feedthrough on the UHV chamber, which is used to actively feed the RF signal into the tunnel junction, and the other connects the spectrum analyzer to the feedthrough, which is used to transfer the amplified RF signal out of the chamber for further analysis. Generally speaking, the thicker the cable is, the lower the insertion loss or attenuation is. Since these cables are used outside of the chamber, the size would not account for a limitation factor in choosing coaxial cables. Therefore, we choose a coaxial cable from MIcable whose insertion loss is smaller than 0.3 dB at 1 GHz.

In the UHV chamber, the choice of coaxial cable is mainly limited by two factors, thermal conductivity and flexibility. For example, the gap voltage line, namely, coaxial cable II, connecting the feedthrough on the top of the chamber at room temperature to the cryostat on the bottom of the inner Dewar at a low temperature must consider the thermal conductivity. In the liquid helium experiment, the temperature of the cryostat is 4.2 K. If the voltage line is made of pure copper wire with a diameter of 1 mm and is 1.3 m long, then the heat flow can be calculated to be 400 kW/m $\times$ $\pi/4$ $\times$ 1 mm^2/1.3 m = 241 mW. Here, the typical value of integral thermal conductivity for pure copper from 300 K to 4 K of 400 kW/m is used. Since the latent heat of vaporization of liquid helium is relatively low, a heating power of 241 mW would consume 0.34 liter of liquid helium per hour. Besides, the heat from ambient environment also induces a thermal drift during STM imaging simply because the tip and sample cannot keep cold. Therefore, we must choose cryogenic cable made of beryllium copper, constantan, or stainless steel. In our case, the material of coaxial cable II (insertion loss: 6.3 dB/m at 1 GHz) is chosen to be stainless steel from HUBER+SUHNER. Aside from the thermal conductivity, the cable directly connecting the buffer amplifier board, namely, coaxial cable III, as shown in Fig. 1(b), should be soft enough to avoid any vibration. Regarding coaxial cable IV, since the two cryogenic amplifiers, CITLF 3, are fixed, a semirigid coaxial cable is used. Here, coaxial cable III (insertion loss: 3 dB/m at 1 GHz) purchased from Lakeshore is made of stainless steel, while coaxial cable IV (insertion loss: 1.4 dB/m at 1 GHz) purchased from Keycom is made of beryllium copper.

Among all of the coaxial cable assemblies used, I, II, and IV are commercially available, whereas cable III is assembled in our lab. Before soldering cable III on the buffer amplifier board, we peel off most of the Teflon jacket because this plastic layer is somewhat rigid, especially at low temperatures, and can cause unwanted vibrations. Part of the Teflon jacket is kept to hold the outer braided stainless steel wires in place because a loose outer metallic shielding mesh may cause a deviation of characteristic impedance from standard 50 Ω. In addition, a lead-free solder (Sn96.5Ag3Cu0.5) instead of regular tin-lead solder is used to avoid outgassing. During the soldering, we find the stainless steel not solderable with tin alloys. Therefore, we dip it into phosphoric acid for about 2 min, then shortly rinse the acid away, and solder it on the buffer amplifier board subsequently after the surface activation.

Apart from the coaxial cables, six power cords in total are also needed to provide DC bias voltages for all of the amplifiers. Based on the same consideration, namely, to maintain the cryogenic environment inside the analysis chamber of STM, we choose the constantan wires with a diameter of 0.254 mm as the power lines. Heat flow through a 1-m-long line from 300 K to 4 K is calculated to be 0.26 mW, which is two orders of magnitude less than that of pure copper wire of the same size. To obtain good electrical contacts, the connectors are assembled on the wires with a specific crimping tool. All of the power cords are connected to a 9 pin sub-D feedthrough. A male to female sub-D adapter from Amphenol with an internal filter whose capacitance is 5600 pF is installed on the air side of the feedthrough. This adapter is intended for filtering out the high-frequency noises in the voltages provided by the external power source.

Finally, all of the coaxial cables and the power cords are bundled up with thin stainless-steel tubes so that they cannot move nor introduce undesired vibrations. These stainless-steel tubes are attached on the outside wall of the inner Dewar by spot-welding. After the replacement of original conducting wires with RF-compatible coaxial cables, RF frequencies up to gigahertz can propagate through the whole instrument without suffering much loss.

C. Impedance matching network and buffer amplifier

Both the DC and RF components in the tunneling current are used in our RF-STM. Therefore, a bias tee, which can separate the DC and RF components in the tunneling current, is necessary in the very front of the signal recovery system. The DC component is then fed into the STM control unit so that the STM can perform imaging and acquire the I(V) spectra, while the RF component, which carries the fast dynamic information, is transferred to the subsequent amplifiers.

To achieve the maximum power transfer from the tunnel junction to the 1st stage amplifier, the input impedance of the amplifier should be designed to be the complex conjugate of the source impedance of the tunnel junction. However, an accurate understanding of the source impedance is not available so far. In many cases, as shown in Fig. 2(a), the tunnel junction can be modeled as a large resistor R_T with a typical resistance of 100 MΩ in parallel with a capacitor whose capacitance is dominated by the stray capacitance (a typical value reported in the literature is 1 pF[20]). The tunneling capacitance C_{TS}, which is dependent on the separation between the tip and sample surface and is in the femtofarad regime,[21] can thus be neglected. Therefore, the source impedance can be calculated by $R_T//-j\omega C_{Stray}$.

Before entering the input port of the 1st stage amplifier, the RF signal passes through the tip and subsequent connecting cable, which introduces a tip body to the grounded scanner stage capacitance C_B and a connecting wire to grounded metallic shield capacitance C_C, respectively. Therefore, the impedance from the tunnel junction seen by the 1st stage amplifier is given by[19]

$$Z_{TJ}(d) = Z_0 \frac{Z_{TJ} + jZ_0 \tan(\beta d)}{Z_0 + jZ_{TJ} \tan(\beta d)}. \quad (1)$$

Here, $Z_{TJ} = R_T//-j\omega(C_{Stray} + C_B + C_C)$ is the impedance of the tunnel junction with parasitic capacitances, Z_0 is the characteristic impedance of connection cable, d is the length of connection cable, and β is the wavenumber.

Concerning the positions of the 1st stage amplifier, there are two possible configurations of installation. The first configuration, as shown in Fig. 2(b), brings less change on the original scanner, which preserves the *in situ* tip exchange function. However, the original tip holder has a much larger area than that of a tip and hence a

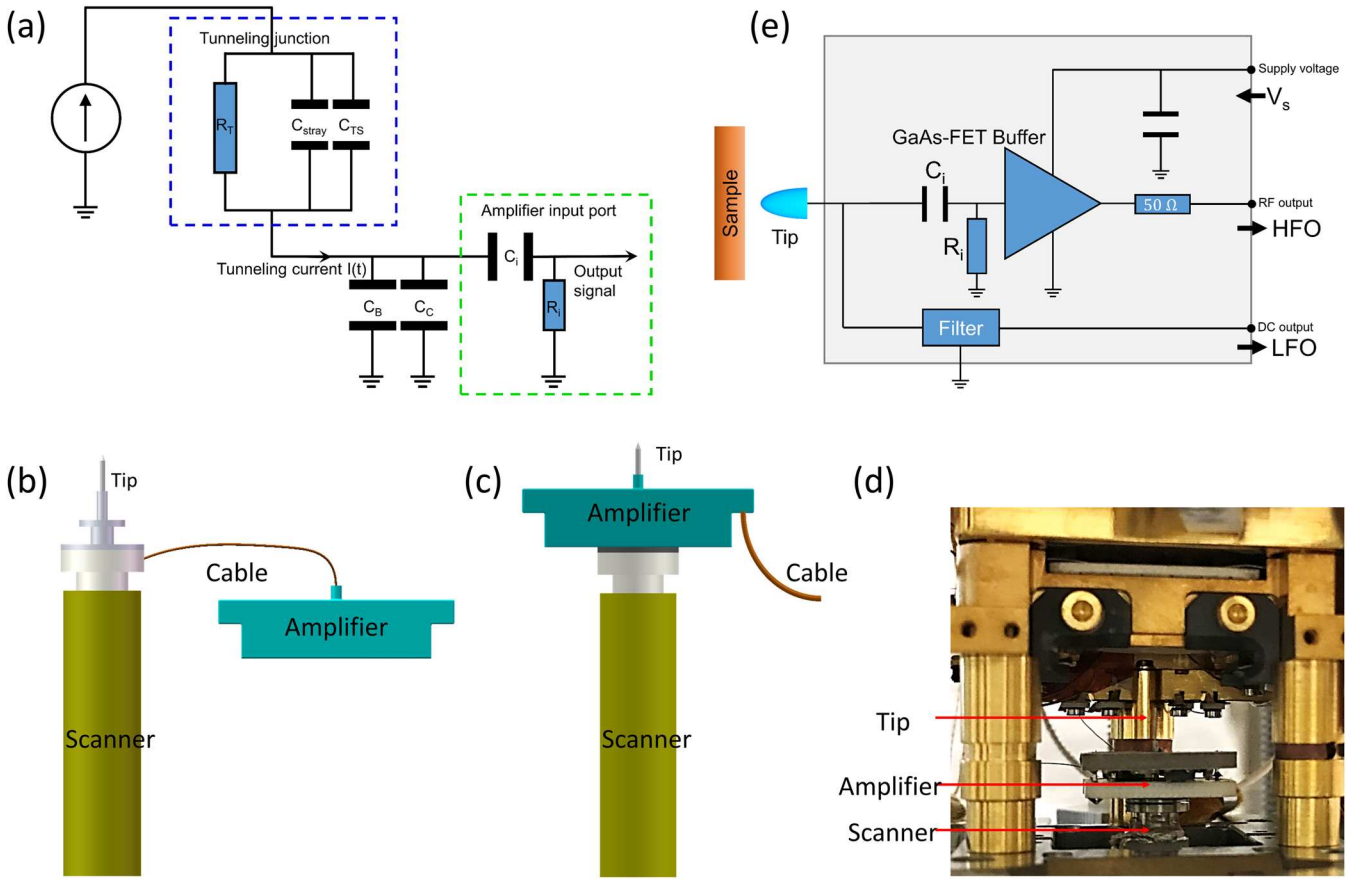

FIG. 2. (a) Equivalent electric circuit of the tunneling junction and the input port of the 1st stage amplifier. Two different configurations for installment of the 1st stage amplifier: (b) 1st stage amplifier is connected to the probe tip via a short cable and (c) 1st stage amplifier is served as the tip holder. (d) Photo of the 1st stage amplifier sitting on top of the scanner tube. (e) Simplified schematic diagram of our 1st stage RF amplifier.

much larger tip body parasitic capacitance C_B. Besides, the unavoidable utilization of a short wire to connect the tip and the amplifier increases the connection capacitance C_C and creates a varied input impedance with frequency originating from the term $\tan(\beta d)$ in Eq. (1). In the second configuration, the tip is integrated directly into the amplifier, as shown in Fig. 2(c), to minimize the tip body parasitic capacitance and eliminate the connection capacitance. It should be also noted that in this configuration, $\beta d = 0$ implies that the impedance from the tunnel junction seen by the 1st stage amplifier is always equal to Z_{TJ}, which is a good condition to design the 1st stage amplifier. Therefore, the second configuration is adopted in our design, as shown in Fig. 2(d), although this configuration does not allow the *in situ* tip exchange. On the other hand, its apparently much bigger size ($18.1 \times 14.6 \times 6$ mm^3) than the original tip holder (diameter of 5 mm and height of 5 mm) limits the coarse motion range of the scanner in both x and y directions (from 10 mm to 5 mm). Although the buffer amplifier is about 2.4 g, 8 times higher than that of the original one (about 0.3 g), it does not affect the overall performance of the STM scanner.

The 1st stage amplifier consists of a low noise PHEMT (pseudomorphic high electron mobility transistor) based on GaAs (Gallium Arsenide) semiconductor technology, which allows for operation at a cryogenic temperature down to 4 K and strong magnetic fields up to 5 T. Figure 2(e) presents the schematic diagram of the internal circuit of this amplifier. The input impedance of this buffer amplifier is given by a resistor R_i of 70 kΩ parallel with an effective input capacitance C_i of 1.9 pF, which together form a high-pass filter whose cut-off frequency is given by $f_c = \frac{1}{2\pi RC} = 1.2$ MHz. The core part of the 1st stage amplifier, namely, the PHEMT, is in common-drain configuration. Ideally, the input voltage is transferred in a 1:1 ratio from input to output (that is why we also call this 1st stage amplifier as the "buffer amplifier"). With a RF current signal I, a RF input voltage U is determined by Ohm's law $U = I \cdot Z$, where $Z = 1/\omega C_i$ is the impedance of input capacitance (for f above 10 MHz). Taking into account a factor of 1.5 for internal attenuations, the actual output *RF* voltage from the 1st stage amplifier would be given by $U = 2/3 \cdot I/2\pi fC$, as a good approximation.

For the range of frequency of interest (10–1000 MHz), the input current noise of our designed amplifier is less than 1.0 pA/$\sqrt{\text{Hz}}$, substantially better than that with a normal 50 Ω input resistance, which generates approximately 2.2 pA/$\sqrt{\text{Hz}}$ thermal noise even at 4.2 K environment as calculated by the Nyquist formula. The latter number assumes even perfect thermalization, which is very hard to achieve in a real-world cryostat. Therefore, the usage of a high impedance buffer stage in conjunction with a good subsequent amplifier of 50 Ω input impedance yields a greatly improved S/N ratio for all frequencies below 1 GHz.

Compared with most commercial cryogenic amplifiers, power consumed by our buffer amplifier under normal operation (supply voltage $V_s = 1.75$ V) is as low as 3.5 mW (e.g., power of the RF amplifier used in the literature[19] is 30 mW), which causes a rather mild thermal heating on our STM. In addition, to avoid any potential damage to the buffer amplifier, we add a protection diode in front of it so that the voltage pulse commonly applied to the tunnel junction to induce a small-scale tip field emission for tip cleaning can be retained during the STM operation. To summarize, we have successfully integrated the bias tee, the impedance matching network, and the buffer amplifier into one single device. This customized buffer amplifier specially designed for STM application is now commercially available in Stahl-Electronics company.

D. RF cryogenic amplifier

After the conversion from current to voltage, the buffered signal is guided to a subsequent low noise amplifier. The RF amplifier used in our setup is a SiGe low noise amplifier intended for extremely low noise cryogenic applications. The amplifier utilizes resistive feedback to achieve good input match and high gain stability. The amplifier is optimum for the frequency range from 0.01 to 2 GHz but is useable to 5 GHz. It is powered from a single positive

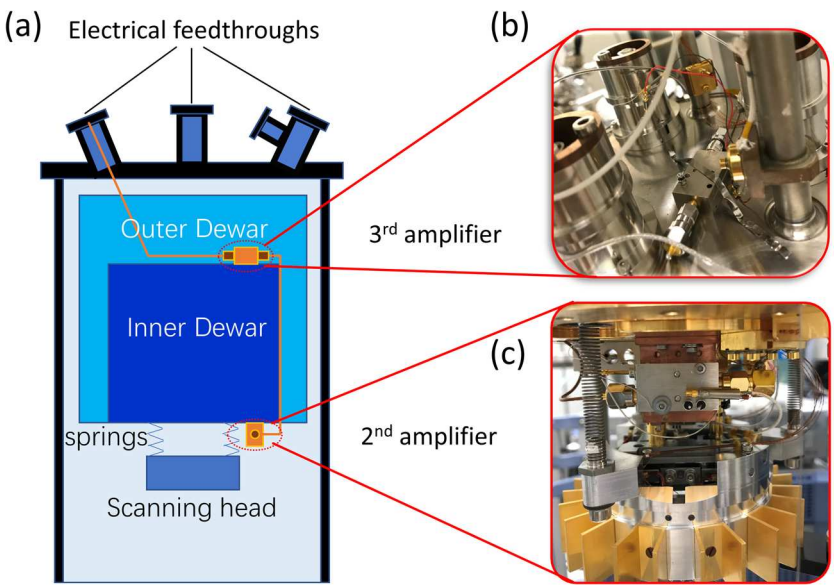

FIG. 3. Mounting positions of two CITLF3 amplifiers in our setup.

DC supply usually 2 V but can be changed to trade off power dissipation and performance. To obtain considerable large amplification, we install two CITLF3 amplifiers in series in our setup.

Sufficient thermal anchoring is crucial to achieve the optimal performance of each cryogenic amplifier. Therefore, the first CITLF3 amplifier is mounted on the bottom of the inner Dewar and the heat generated during its operation is directly transferred to the cryostat via an oxygen-free copper bracket. The second CITLF3 amplifier is attached tightly on top of the inner Dewar, as shown in Fig. 3. We expect that this configuration would deliver a nearly perfect cooling effect.

III. PERFORMANCES TESTS

A. STM imaging

After installing all of the necessary components, including the impedance matching network, two stage cryogenic low noise RF amplifiers in series, and a high-end spectrum analyzer, our LT-STM is successfully upgraded to a RF-STM. In addition, this instrument is housed in a newly built RF shielding room that can provide effective shielding as high as 20 dB. The first test of our constructed RF-STM is regarding the basic STM operation, namely, STM imaging.

The test is performed on a clean Au(111) surface. As we mentioned before, the buffer amplifier actually serves as the tip holder in our RF-STM, which is not fixed but magnetically attached on top of the scanner tube via a small magnetic base. To make things worse, a short cable with a somewhat rigid plastic shielding is connected on the buffer amplifier board. One might expect that the imaging ability will be deteriorated to some extent. Figure 4(a) shows the image of the Au(111) surface acquired by this newly built RF-STM in the constant-current mode. We can observe the characteristic herringbone reconstruction features on the Au(111) surface clearly. With a good tip, the STM images with atomically resolved atoms can also be obtained at specific tunneling conditions, as shown in Fig. 4(b). To quantify the tip stability in the vertical direction during imaging, we freeze the tip at the tunneling position and keep the feedback loop on to satisfy the constant current condition. It can be expected that the piezo will drive the motion of the tip to compensate the variation of tip-sample separation. Therefore, the tip position z(t) can serve as the indicator of the tip stability.

Figure 4(c) shows the tip position $z(t)$ in frequency domain featuring several peaks in the spectrum. We can notice that none of the peaks exceeds 3.5 pm/$\sqrt{}$Hz. Moreover, analysis of the tip position $z(t)$ can give us a hint about the major vibration sources of the probe tip during scanning. It can be noted that the frequencies of noises are lower than 400 Hz. Generally speaking, two kinds of noises will contribute to the instability of the STM tip. One originates from the AC power supply, namely, the power-line noise, a 50 Hz electrical noise, and its low harmonics, while the other arises from certain mechanical vibrations, in most cases, caused by direct contact of the suspension system of the scanning head with the surrounding rigid objects, such as the wall of the Dewar and the copper shield.

To minimize the former noise, ground loops formed by multiple paths to ground should be eliminated. If we look at the noise spectrum presented in Fig. 4, we can find that the noises should not come from electrical noise but mechanical vibrations. Since the scanning head is suspended by three springs and kept upright to avoid any contacts with surrounding objects, we believe the frequencies appeared in the noise spectrum is caused by the coaxial cable connecting the buffer amplifier and the subsequent RF amplifier.

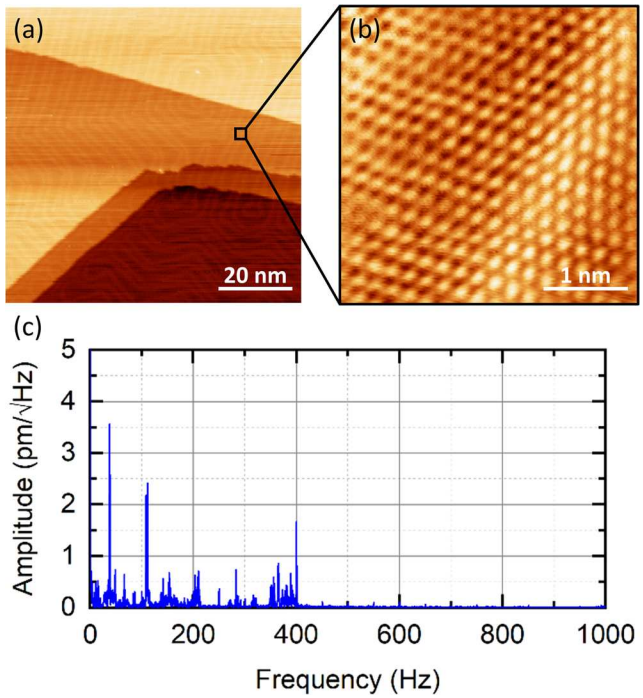

FIG. 4. (a) Constant-current STM image of the reconstructed Au(111) surface, showing the characteristic herringbone structure and several atomic steps. (b) Enlarged atomically resolved STM image of a 3.5 nm × 3.5 nm area on the Au(111) surface, denoted by a black box in (a). Tunneling conditions for (a) and (b) are −1.0 V, 200 pA and −0.05 V, 30 pA, respectively. (c) Tip position $z(t)$ is represented in the frequency domain.

To summarize, although there could be less loss in signal transmission from the tunnel junction to the subsequent signal detection system by positioning the buffer amplifier as close to the sample as possible, it is at the price of a relatively large vibration level during scanning. Nevertheless, the vibration level (~10 pm) still allows for the imaging of most nanostructures whose typical size are in the angstrom regime, such as individual atoms and molecules, self-assembled organic molecular monolayers, and nanosized islands.

B. RF performances of the signal recovery system

Now, it is time for us to evaluate the RF performance of this RF-STM. Instead of switching on all of the amplifiers at the same time, we switch them on backwards sequentially and perform the frequency sweep. Figure 5 presents the power spectra acquired by the spectrum analyzer. When all of the amplifiers are powered off, we can observe a periodic feature (the interval Δf between two neighboring peaks is 41.8 MHz) in the power spectrum. Each peak represents the presence of a standing wave inside the coaxial cables between the spectrum analyzer and the 3rd stage amplifier. Here, the powered-off 3rd stage amplifier creates open-circuited condition under which the thermal noise is no longer "white" but

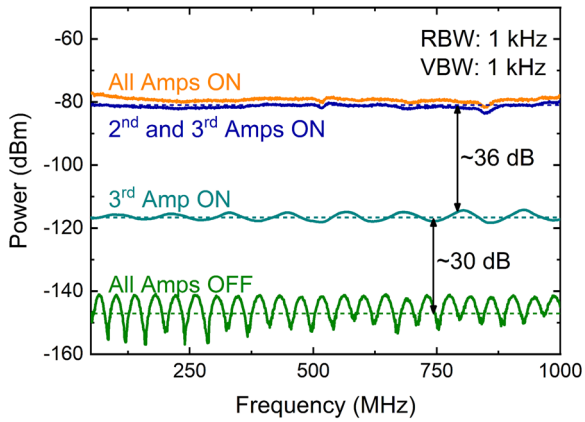

FIG. 5. Power spectra acquired by the spectrum analyzer by turning on the amplifiers sequentially. In these measurements, the resolution bandwidth (RBW) and video bandwidth (VBW) are set to the same value.

frequency-dependent. The wavelengths of these maxima satisfy

$$l = \left(\frac{1}{4} + \frac{1}{2}\cdot n\right)\lambda, \quad n = 0, 1, 2, \ldots, \tag{2}$$

where l is the length of the coaxial cable, with their corresponding resonant frequencies $f_n = \frac{v}{\lambda} = \frac{v}{l}\left(\frac{1}{4} + \frac{1}{2}\cdot n\right)$ (v is the propagation speed of the RF signal in the coaxial cables). The amount of time the signal takes to travel from one end to the other end of this cable is determined by $l/v = 1/2\Delta f = 12.0$ ns.

Similarly, when the 3rd stage amplifier is powered on, the standing wave occurs in the coaxial cable between the 3rd stage amplifier and the 2nd stage amplifier. Since this coaxial cable is shorter, the interval Δf between two neighboring peaks shown in the power spectrum is larger. From Δf = 117.9 MHz, we can obtain the signal travel time in this cable to be 4.24 ns. The much shorter coaxial cable III (~5 cm) between the 2nd stage amplifier and the 1st stage buffer amplifier can only sustain standing waves of much shorter wavelength with much higher frequencies. Therefore, the periodic feature is no longer observable in the power spectrum within the observed frequency range (up to 1 GHz) after the 2nd stage amplifier is powered on. In addition, from these power spectra, we can also obtain the power gains of each amplifier, namely, 30 dB for the 3rd stage amplifier and 36 dB for the 2nd stage amplifier. It should be noted that although the 2nd and the 3rd stage amplifiers are the same, the different surrounding temperature may cause different power gain.

C. RF-sensitivity of our RF-STM setup

The power spectral density S_f of the tunneling current noise is given by the following equation:[9]

$$S_f = 2eI_T \coth\left(\frac{eI_TR_T}{2k_BT}\right), \tag{3}$$

where e is the elemental charge, I_T is the tunneling current, R_T is the resistance of the tunnel junction, k_B is the Boltzmann constant, and T is the physical temperature. It should be noted that when $eI_TR_T \gg k_BT$, the tunneling current noise is mainly contributed by the shot noise where the noise power density is proportional to the amplitude of tunneling current; when $eI_TR_T \ll k_BT$, the thermal noise becomes dominant where the noise power density does not depend on the tunneling current any more.

In our noise measurements, we first control the tip at a specific position above a clean Au(111) surface using the convention STM electronics that can provide a stable measurement condition, namely, to maintain a constant DC resistance of the tunneling junction. In our case, the DC resistance value is set to 1 MΩ. Then, we measure the noise power passing through a specific frequency range, namely, 4.5–5.5 MHz. When the set DC tunneling current value is varied, the bias voltage is adjusted correspondingly to maintain the DC resistance as 1 MΩ.

After removing the excess noise that comes from the amplifiers, the normalized noise power density can be fitted by Eq. (3) using these three temperatures, 300 K, 78 K, and 5.3 K. The experimental results and the fitting lines are presented in Fig. 6. We can see that at room temperature, the noise power is the mixture of shot noise and thermal noise, while at liquid nitrogen and helium temperatures, the shot noise dominates, especially in the high tunneling current regime. The temperature-dependent noise power density lays a foundation for noise-based thermometry. The effective temperature extracted from the noise power should be the average of tip temperature and sample surface temperature.[9] In principle, our RF-STM can be used to perform a thermal imaging on the sample surface of interest to measure the local temperature variance with an unprecedented spatial resolution.

When it comes to the sensitivity measurement, we need a reliable RF signal generator to perform the simulation of a signal source positioned inside the tunnel junction. Here, the existing RF signal generator located outside the chamber is not suitable because it is very difficult to determine the exact value of the bias voltage applied on the tunnel junction. Therefore, we decide to use the intrinsic

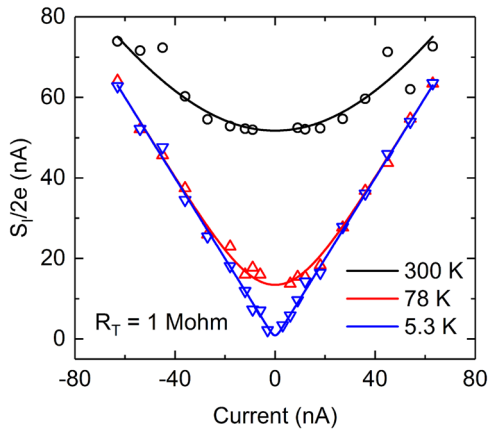

FIG. 6. Normalized power spectral density of the tunneling current noise measured at three typical temperatures, 300 K (room temperature), 78 K (liquid nitrogen temperature), and 5.3 K (liquid helium temperature, not 4.3 K because of the heating from the buffer amplifier). The DC resistance of the tunneling junction is fixed at R_T = 1 MΩ when the set DC current is varied by adjusting the set DC voltage accordingly.

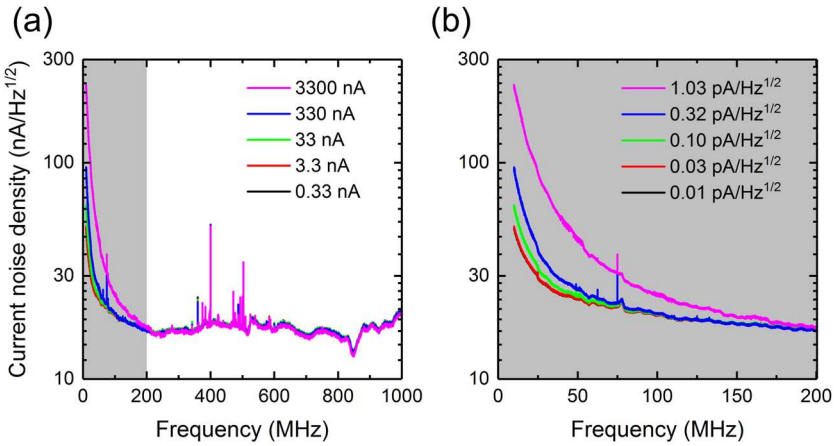

FIG. 7. Sensitivity measurement of our RF-STM in RF band. (a) Current noise spectral density measured by the spectrum analyzer in the frequency range from 10 to 1000 MHz at varied tunneling current. The legend presents the values of the tunneling current. (b) Zoomed-in view of the spectra of panel (a). The legend presents the amplitudes of shot noise generated by these tunneling currents, which are calculated with the formula $\sqrt{\langle \Delta I^2 \rangle} = \sqrt{2eI_T \cdot RBW}$, a limit form of Eq. (3) in the high current limit. Here, RBW is the resolution bandwidth used in the measurement. All of the spectra are acquired at 78 K.

shot noise introduced by the tunneling current as the RF signal "generator." This RF signal source has three unique advantages. First, its location inside the tunnel junction helps circumvent the impedance mismatch between the tunnel junction and the coaxial line that connects to the external RF signal generator. Second, it has a "white" power density spectrum over a very wide frequency range. Third, the amplitude of the shot noise can be easily adjusted by varying the tunneling current whose stability can thus be guaranteed by the STM feedback system. However, the maximum power of this "signal source" is really small because a higher tunneling current implies a stronger electrical field between the tip and the sample surface, leading to field electron emission. In our case, the maximum stable current noise spectral density of the shot noise can reach about 1.03 pA/$\sqrt{\text{Hz}}$, corresponding to a tunneling current of 3300 nA.

Figure 7 presents the sensitivity measurement results of our RF-STM. It can be seen that when the shot noise in the tunnel junction is very weak, it would submerge in the thermal noise background induced by the subsequent electronic devices, mainly, the 1st and 2nd stage amplifiers. As the amplitude of the shot noise increases, it would gradually appear on the spectra. For the same shot noise source, as the frequency increases, the shot noise in the tunnel junction becomes indistinguishable from the thermal noise of the subsequent devices as well. More importantly, we conclude from this figure that our RF-STM can resolve any signal source whose amplitude exceeds 1.0 pA/$\sqrt{\text{Hz}}$ in the frequency range up to 200 MHz. This is consistent with the estimated value. These numbers represent at least one order of magnitude better than those of the experimental setups from other groups.[10,22]

IV. CONCLUSION

To summarize, we have developed a RF-STM with high sensitivity. The most critical part in this work is to design and install an active IMN, the buffer amplifier, with an internal bias tee to separate the high frequency and DC components in the tunneling current. This FET-based buffer amplifier provides impedance matching over a broad bandwidth as high as 1 GHz. In addition, to complete the signal recovery system, two cryogenic low noise amplifiers are installed subsequently in series, providing substantial power gain. Finally, the constructed cascade amplifier for the signal recovery can provide considerable amplification (>60 dB) in a frequency range as wide as 1 GHz. Moreover, the tunneling current noise measurement performed by the RF-STM not only demonstrates its potential application in thermometry at atomic scale but also determines its sensitivity level to be about 1.0 pA/$\sqrt{\text{Hz}}$ at 200 MHz at 78 K. This system is intended to be a powerful tool to study fast dynamic physical processes in the tunnel junction.

ACKNOWLEDGMENTS

We acknowledge the technical support on the design and fabrication of the buffer amplifier of Dr. Stahl from Stahl Electronics. This work was supported by the Research Grant Council of Hong Kong (Grant No. 404613), the Direct Grant for Research of CUHK (Grant Nos. 4053306 and 4053348), the National Natural Science Foundation of China (Grant No. 11574128), and the MOST 973 Program (Grant No. 2014CB921402).

REFERENCES

[1] G. Binnig and H. Rohrer, Rev. Mod. Phys. **59**(3), 615 (1987).
[2] D. P. Smith and G. Binnig, Rev. Sci. Instrum. **57**(10), 2630–2631 (1986).
[3] G. Binnig, H. Rohrer, C. Gerber, and E. Weibel, Phys. Rev. Lett. **50**(2), 120 (1983).
[4] V. Hallmark, S. Chiang, J. Rabolt, J. Swalen, and R. Wilson, Phys. Rev. Lett. **59**(25), 2879 (1987).
[5] R. Hamers, R. Tromp, and J. E. Demuth, Phys. Rev. Lett. **56**(18), 1972 (1986).
[6] J. A. Stroscio, R. Feenstra, and A. Fein, Phys. Rev. Lett. **57**(20), 2579 (1986).
[7] R. Wolkow and P. Avouris, Phys. Rev. Lett. **60**(11), 1049 (1988).
[8] S. Pan, E. Hudson, K. Lang, H. Eisaki, S. Uchida, and J. Davis, Nature **403**(6771), 746 (2000).
[9] U. Kemiktarak, T. Ndukum, K. C. Schwab, and K. L. Ekinci, Nature **450**(7166), 85 (2007).
[10] Y. Manassen, R. J. Hamers, J. E. Demuth, and A. J. Castellano, Phys. Rev. Lett. **62**(21), 2531–2534 (1989).
[11] C. Durkan and M. E. Welland, Appl. Phys. Lett. **80**(3), 458–460 (2002).
[12] S. Müllegger, M. Rashidi, K. Mayr, M. Fattinger, A. Ney, and R. Koch, Phys. Rev. Lett. **112**(11), 117201 (2014).
[13] S. Baumann, W. Paul, T. Choi, C. P. Lutz, A. Ardavan, and A. J. Heinrich, Science **350**(6259), 417–420 (2015).

[14]S. Müllegger, S. Tebi, A. K. Das, W. Schöfberger, F. Faschinger, and R. Koch, Phys. Rev. Lett. **113**(13), 133001 (2014).
[15]F. D. Natterer, K. Yang, W. Paul, P. Willke, T. Choi, T. Greber, A. J. Heinrich, and C. P. Lutz, Nature **543**(7644), 226–228 (2017).
[16]P. Willke, Y. Bae, K. Yang, J. L. Lado, A. Ferrón, T. Choi, A. Ardavan, J. Fernández-Rossier, A. J. Heinrich, and C. P. Lutz, Science **362**(6412), 336–339 (2018).
[17]F. D. Natterer, F. Patthey, T. Bilgeri, P. R. Forrester, N. Weiss, and H. Brune, Rev. Sci. Instrum. **90**(1), 013706 (2019).
[18]Y. Sainoo, H. Isshiki, S. M. F. Shahed, T. Takaoka, and T. Komeda, Appl. Phys. Lett. **95**(8), 082504 (2009).
[19]P. Messina, F. Fradin, and P. Pittana, Nanotechnology **20**(5), 055705 (2009).
[20]D. T. Lee, J. Pelz, and B. Bhushan, Rev. Sci. Instrum. **73**(10), 3525–3533 (2002).
[21]J. Hou, B. Wang, J. Yang, X. Wang, H. Wang, Q. Zhu, and X. Xiao, Phys. Rev. Lett. **86**(23), 5321 (2001).
[22]P. Messina, M. Mannini, A. Caneschi, D. Gatteschi, L. Sorace, P. Sigalotti, C. Sandrin, S. Prato, P. Pittana, and Y. Manassen, J. Appl. Phys. **101**(5), 053916 (2007).